ADVANCED MATERIALS
www.advmat.de

Edge-Epitaxial Growth of 2D NbS_2-WS_2 Lateral Metal-Semiconductor Heterostructures

Yu Zhang, Lei Yin, Junwei Chu, Tofik Ahmed Shifa, Jing Xia, Feng Wang, Yao Wen, Xueying Zhan, Zhenxing Wang, and Jun He**

2D metal-semiconductor heterostructures based on transition metal dichalcogenides (TMDs) are considered as intriguing building blocks for various fields, such as contact engineering and high-frequency devices. Although, a series of p–n junctions utilizing semiconducting TMDs have been constructed hitherto, the realization of such a scheme using 2D metallic analogs has not been reported. Here, the synthesis of uniform monolayer metallic NbS_2 on sapphire substrate with domain size reaching to a millimeter scale via a facile chemical vapor deposition (CVD) route is demonstrated. More importantly, the epitaxial growth of NbS_2-WS_2 lateral metal-semiconductor heterostructures via a "two-step" CVD method is realized. Both the lateral and vertical NbS_2-WS_2 heterostructures are achieved here. Transmission electron microscopy studies reveal a clear chemical modulation with distinct interfaces. Raman and photoluminescence maps confirm the precisely controlled spatial modulation of the as-grown NbS_2-WS_2 heterostructures. The existence of the NbS_2-WS_2 heterostructures is further manifested by electrical transport measurements. This work broadens the horizon of the in situ synthesis of TMD-based heterostructures and enlightens the possibility of applications based on 2D metal-semiconductor heterostructures.

Being a striking member in the family of transition metal dichalcogenides (TMDs), bulk metallic TMDs have gained significant attention over the past few years due to their intriguing properties, such as superconductivity,[1–3] unique magnetism,[4,5] Mott transition (metal to nonmetal transition),[2] and charge density wave (CDW).[6–8] Recently, abundant researches based on 2D layered semiconductor TMDs, such as MoS_2,[9–11] $MoSe_2$,[12] ReS_2,[13] $MoTe_2$,[14] etc., have revealed remarkable electrical and optical properties. Beside this, metallic TMDs (TaS_2, VS_2, $NbSe_2$, etc.) have also stirred up research interest with their typical dichalcogenide analogous for exploring their indispensible contribution to the gorgeous world.[15–18] In their 2D limit, the phenomena of superconductivity, CDW order, and phase transition are still maintained.[5,19–21] Moreover, these 2D metallic materials with no bandgap and outstanding electrical conductivity forecast lots of potential applications, such as transparent electrode,[22] efficient electrode contact for 2D semiconductor device,[23–26] and electrocatalysis.[27] However, in contrast to semiconductor TMDs, exciting explorations have been rarely communicated about 2D metallic TMD nanosheets hitherto. This can be attributed to the lack of controllable preparation of high-quality 2D metallic TMD nanosheets.

Niobium disulfide (NbS_2), with a layered structure, is a typical member of metallic TMDs. It is attractive for its superconductivity and unique collective electronic states, as well as its optical and magnetic properties.[28–34] Furthermore, the metallic nature endows excellent electronic transport ability, which in turn finds a remarkable application as electrode contact in electronic devices. As it is well known, 2D TMD semiconductors have been widely used in electronic devices, but their performance is significantly hindered by the electrode contact.[26] Recently, theoretical calculations have indicated that 2D metal-semiconductor junctions can weaken the Fermi level pinning and effectively tune the Schottky barrier.[35] And experimental results further confirmed that a heterostructure constructed with a metallic TMD, serving as electrode contact, exhibits a higher mobility and markedly decreased Schottky barrier.[24] On the other hand, Schottky type

Dr. Y. Zhang, L. Yin, J. Chu, Dr. T. A. Shifa, Dr. F. Wang, X. Zhan, Prof. Z. Wang, Prof. J. He
CAS Center for Excellence in Nanoscience
CAS Key Laboratory of Nanosystem and Hierarchical Fabrication
National Center for Nanoscience and Technology
Beijing 100190, China
E-mail: wangzx@nanoctr.cn; hej@nanoctr.cn

L. Yin, Dr. T. A. Shifa, Dr. F. Wang, Y. Wen, Prof. Z. Wang, Prof. J. He
University of Chinese Academy of Science
No.19A Yuquan Road, Beijing 100049, China

J. Chu
State Key Laboratory of Electronic Thin Films
and Integrated Devices
University of Electronic Science and Technology of China
Chengdu 610054, China

J. Xia
key Laboratory of Photochemical Conversion and Optoelectronic
Materials
Technical Institute of Physics and Chemistry
Chinese Academy of Sciences
Beijing 100190, China

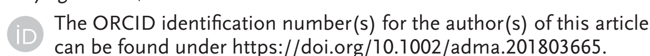
The ORCID identification number(s) for the author(s) of this article can be found under https://doi.org/10.1002/adma.201803665.

DOI: 10.1002/adma.201803665

© 2018 WILEY-VCH Verlag GmbH & Co. KGaA, Weinheim

metal-semiconductor heterostructure maybe also be promising in high-speed integrated circuits and microwave technologies, considering its high-frequency characteristics. Additionally, the ultrathin body thickness of 2D configuration can bring metallic TMDs high mechanical flexibility, which makes the pliable/wearable device systems capable. Hence, the direct synthesis of 2D metal-semiconductor TMD heterostructures is crucial for the practical applications of TMD-based electronic and optoelectronic devices.

Bulk metallic TMD crystals are commonly synthesized via chemical vapor transport techniques[36–38] and their thin flakes are obtained by mechanical exfoliation method.[19] Very few reports about the uniform and controllable growth of monolayer metallic TMDs have been made so far by chemical vapor deposition (CVD) method.[17,20,39] Although lots of interesting physics and electronic properties have been explored from 2D TMD semiconductors and its heterostructures obtained via one-step, two-step, and even multistep growth processes,[40–47] the synthesis of 2D metallic TMDs and establishment of Van der Waals (vdW) heterostructures between metallic and semiconductor TMDs are sparsely reported.[48,49] These have not only hindered the exploration of their electronic/magnetic properties but also greatly impeded their practical applications in electronic devices.

Having in mind the astonishing research progress on CVD grown high-quality and large domain MoS_2, WS_2 flakes, etc.,[50–52] and also speculating the similar structure of NbS_2 with a complementary electronic properties, it is reasonable to hypothesize that the rational synthesis of NbS_2-WS_2 heterostructures could lead us one step forward in the area of 2D materials. In this study, we present a direct synthesis of monolayer NbS_2 with a large domain size via an ambient pressure CVD (APCVD) method. More importantly, we realize a controllable epitaxial growth of NbS_2-WS_2 lateral heterostructures via a facile "two-step" CVD route. Transmission electron microscopic studies show perfect atomic structures and clear chemical modulation with distinct interfaces. Moreover, Raman and photoluminescence (PL) spectroscopic characterizations reveal the controlled spatial modulation within the concentric triangular domain such that the central part is composed of WS_2 triangle and the peripheral region consisting of NbS_2. Using our CVD-grown NbS_2-WS_2 lateral heterostructures, we fabricated field-effect transistors (FETs) wherein the electrical transport measurements demonstrate explicit Schottky junction features with well-defined rectification, which indicate the potential application in electronic devices. We believe that the findings in our work pave a promising way for the property investigations and application developments of 2D metallic materials and 2D metal-semiconductor TMD heterostructures.

Uniform monolayer metallic NbS_2 triangles were grown on sapphire (Al_2O_3(0001)) substrates via an APCVD system in a three-zone furnace. Niobium pentoxide (Nb_2O_5) and Sulfur (S) powder were chosen as the reaction precursors. The Nb_2O_5 powder, mixed with a little amount of Sodium chloride (NaCl), was placed at the center of quartz tube onto which the growth substrate (sapphire(Al_2O_3(0001))) was laid facing down. The sulfur powder was then placed at the upstream region. The reaction condition was set in such a way that the temperature of the upstream region was raised to 150–200 °C, and the sulfur vapor was carried by Ar gas flow (mixed by H_2) toward the center to react with Nb_2O_5 at 790 °C and deposit NbS_2 on sapphire. More details of the growth experiments are provided in the Experimental Section and Supporting Information (Figure S1). **Figure 1**a schematically depicts the typical structure model of monolayer NbS_2 seen from top and side views, which is similar to that of MoS_2.[9] A typical scanning electronic microscopy (SEM) image in Figure 1b demonstrates the achievement of uniform NbS_2 triangles on sapphire. And the maximum edge length of the as-grown NbS_2 triangle can be as large as 100 µm, confirmed by the inset optical image. Furthermore, X-ray photoelectron spectroscopy (XPS) results and Raman spectra of as-grown monolayer NbS_2 were also obtained and supplemented in Figures S2 and S3 (Supporting Information), fully confirming its chemical component. Figure 1c gives a representative atomic force microscopy (AFM) image and demonstrates that the thickness of as-grown NbS_2 triangles is ≈1.0 nm, indicating its monolayer nature. Besides, the as-grown NbS_2 is proved to be air-stable (Figure S4, Supporting Information). Afterward, the NbS_2-WS_2 lateral heterostructure was fabricated by sequentially growing each components on sapphire (Al_2O_3(0001)) substrates through a "two-step" CVD route, as schematically illustrated in Figure 1d. In the first step, large-scale monolayer WS_2 triangles were synthesized on the sapphire substrate via an APCVD method. Briefly, WO_3 powder, mixed with a little amount of NaCl powder, was used as growth precursor and sulfurized by sulfur vapor to obtain a large scale WS_2 monolayer at 730 °C (details of the growth process are elaborated in Figure S5 in the Supporting Information and the Experimental Section). Subsequently, monolayer WS_2 triangles supported by sapphire substrate were in turn utilized for the preparation of NbS_2 layers. In the second growth step, the APCVD method for the NbS_2 growth (mentioned above) was again adopted to eventually realize the epitaxial growth of NbS_2. Notably, there exists a short interruption before the second growth step for material transition. Generally, the edges or grain boundaries of primary synthesized WS_2 are easily passivated by some impurities under an ambient condition. Merely, the absorbent molecules can be removed by the NbS_2 growth process at a relatively high growth temperature (≈790 °C) under the S atmosphere. So no additional treatment is necessary between the two-step growth processes. Figure 1e shows SEM image of monolayer WS_2 triangle obtained from the first step growth. The XPS and AFM results are shown in Figures S6 and S7 (Supporting Information). The morphology of the lateral heterostructure grown as triangular NbS_2-WS_2 on sapphire substrate can be clearly visualized from the SEM image in Figure 1f. These two concentric triangular regions with a slightly different image contrast marked by yellow and blue triangles reveal a transparent interface between WS_2 (centric) and NbS_2 (peripheral) (the elements' distribution is presented in Figure S16, Supporting Information). The AFM image (inset of Figure 1f) indicates that the heterostructure possesses a smooth surface with a thickness of 10 nm for NbS_2 and a height of ≈1.0 nm for WS_2. Notably, by controlling the growth parameters, the thickness of NbS_2 within the heterostructure can be as thin as about ≈5 nm, shown in Figure S9 (Supporting Information). Furthermore, the chemical composition of NbS_2-WS_2 lateral heterostructure

© 2018 WILEY-VCH Verlag GmbH & Co. KGaA, Weinheim

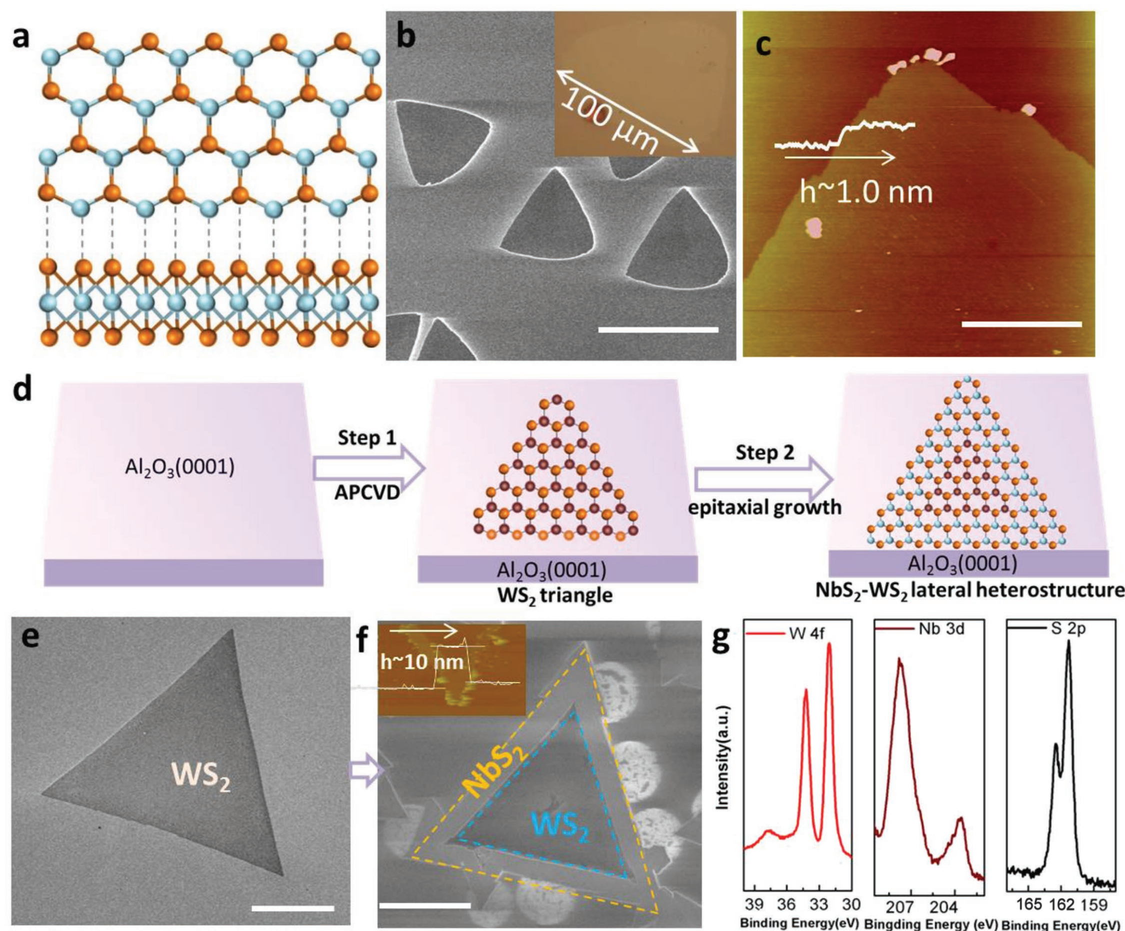

Figure 1. Direct synthesis of monolayer metallic NbS_2 triangles and its heterostructure on sapphire by ambient-pressure CVD method. a) Atomic model of monolayer NbS_2 viewed from different directions, blue and orange balls represent Nb and S atoms, respectively. b) SEM image of uniform NbS_2 crystals grown on a sapphire substrate. Scale bar, 50 μm. Inset shows a monolayer NbS_2 crystal with edge length of 0.1 mm. c) AFM image and its corresponding height profile of a monolayer shows the typical thickness is ≈1.0 nm. Scale bar, 5 μm. d) Schematic illustration of the process of in-plane epitaxial growth of NbS_2-WS_2 lateral heterostructure. e) A typical SEM image of monolayer WS_2 triangles grown by APCVD method. Scale bar, 25 μm. f) SEM image of an NbS_2-WS_2 lateral heterostructure. Scale bar, 20 μm. g) Typical XPS spectra of Nb 3d, W 4f, and S 2p orbitals.

was determined by X-ray photoelectron spectroscopy (XPS) characterization (Figure 1g). It is apparent that the heterostructure constitutes elements of Nb, W, and S. The chemical states of Nb $3d_{5/2}$ and $3d_{3/2}$ can be identified from the peaks at binding energies of 203.5 and 207.5 eV, respectively. The $4f_{7/2}$ and $4f_{5/2}$ states of W are corroborated from the peaks at binding energies ≈32.0 and 34.3 eV whereas those at binding energies ≈161.5 and 162.5 eV are meant for $2p_{3/2}$ and $2p_{1/2}$ states of S, respectively, which are in agreement with the spectra of NbS_2 and WS_2.[41] Besides, by further designing and controlling the growth parameters, NbS_2/WS_2 vertical heterostructures were also successfully obtained via Van der Waals epitaxial growth. And the coverage of upper NbS_2 film can be efficiently controlled by tuning the growth condition. Much more detailed information about their morphologies and optical properties of the NbS_2/WS_2 vertical heterostructures is shown in Figure S10–S12 (Supporting Information). In brief, these results demonstrate that we realize the epitaxial growth of NbS_2-WS_2 heterostructures in both lateral and vertical ways via a "two-step" CVD method.

Atomic resolution transmission electron microscope (TEM) and high-angle annular dark-field scanning transmission electron microscopy (HAADF-STEM) were further performed on transferred samples to investigate the detailed atomic structures of monolayer NbS_2 and NbS_2-WS_2 lateral heterostructure. **Figure 2**a shows a high-resolution TEM (HRTEM) image of NbS_2, displaying a perfect atomic arrangement. The (100) lattice plane spacing (d_{100}) extracted from Figure 2a can be revealed as ≈0.291 nm; thus the in-plane lattice constant (a_0) should be ≈0.336 nm. Figure 2b shows the corresponding selective area electron diffraction (SAED) pattern with only one set of diffraction spots, revealing the single crystalline nature of NbS_2 and its high crystal quality. On the basis of SAED study, we can also determine the (100) lattice plane spacing of NbS_2 to be 0.291 nm, consistent with the one observed from the HRTEM result. Energy-dispersive spectroscopy (EDS) mapping was also employed along with TEM on the transferred samples to identify the chemical composition. Figure 2c,d clearly exhibits the spatial distribution of Nb and S atoms on the triangular corner area and the compositional uniformity of the synthesized NbS_2

© 2018 WILEY-VCH Verlag GmbH & Co. KGaA, Weinheim

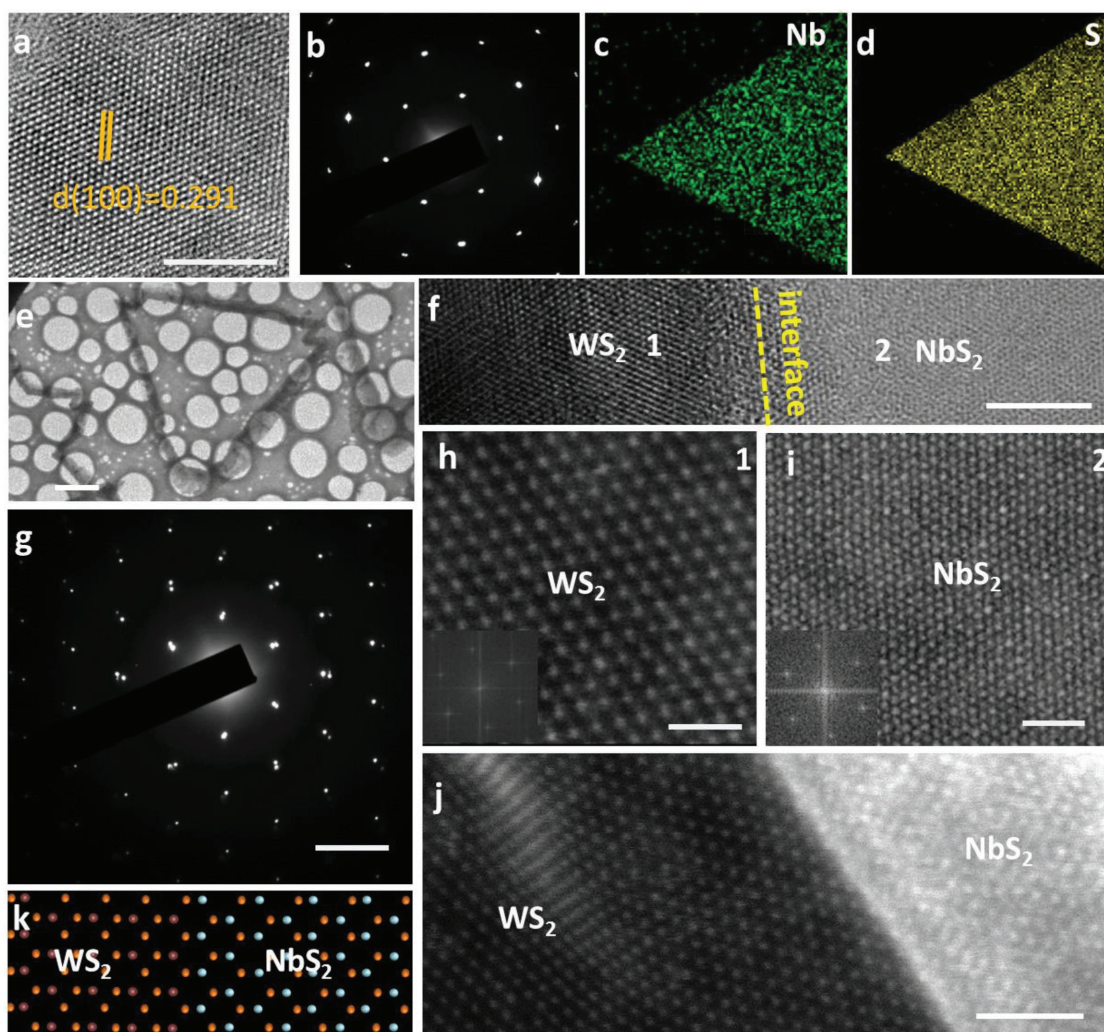

Figure 2. Atomic structure of monolayer NbS_2 and NbS_2-WS_2 lateral heterostructure. a) High-resolution TEM image of a monolayer NbS_2. Scale bar, 5 nm. b) Corresponding SAED pattern captured within a 500 × 500 nm^2 area. c,d) Elemental analysis of the transferred sample by EDS achieved on TEM grids. e) Low-magnification TEM image of a triangular NbS_2-WS_2 lateral heterostructure. Scale bar, 10 µm. f) High-resolution TEM images of the lateral interfaces, Scale bar, 5 nm. g) Corresponding SAED patterns taken from the interface region in (f). Scale bar, 5 nm^{-1}. h) STEM image of WS_2 region away from the interface in (f) marked by 1 and the corresponding fast Fourier transform (FFT) image (as an inset). Scale bar, 1 nm. i) STEM image of the NbS_2 region away from the interface in (f) marked by 2 and the corresponding FFT image (as an inset). Scale bar, 1 nm. j) HAADF-STEM image collected at the interface. Scale bar, 2 nm. k) Associated atomic ball model for the junction in (j).

nanosheet by the uniform color contrasts. Depth insight into the atomic structure and heterointerfaces of NbS_2-WS_2 lateral heterostructure can be gleaned from Figure 2e in which a low-magnification TEM image of an intact triangular NbS_2-WS_2 flake with obvious contrasts is clearly visible. A more distinct feature of the two components (yellow dashed line) between WS_2 (left) and NbS_2 (right) is apparent from the HRTEM image displayed in Figure 2f. A grain boundary can be seen at the heterointerface. And Corresponding TEM-SAED spots obtained from the heterointerface exhibit two sets of hexagonal diffraction pattern spots with no rotation as shown in Figure 2g, highly indicative of the same crystal orientation and an edge-epitaxial growth of NbS_2-WS_2 lateral heterostructure. Thus, HAADF-STEM was further utilized to reveal the atomic structure and heterointerface. The STEM images taken from regions 1 and 2 away from the heterointerface, as shown in Figure 2h,i, demonstrate the individual WS_2 and NbS_2 regions with perfect hexagonal arrangements, confirming the high crystalline quality of our CVD-grown materials. The extracted (100) lattice plane spacings of 0.277 and 0.291 nm are in agreement with the values for pure WS_2 and NbS_2, respectively. And corresponding fast Fourier transformation (FFT) analysis of each side shows only one set of hexagonally arranged spot, respectively, verifying the individual chemical component of WS_2 (left) and NbS_2 (right) (Figure S13, Supporting Information). Figure 2j exhibits a smooth atomic arrangement at the interface between WS_2 and NbS_2 (Figure S14, Supporting Information). The corresponding atomic model in Figure 2k also schematically simulates the distinct interface connection between NbS_2 and WS_2. Together, these TEM studies reveal the explicit chemical modulation in our NbS_2-WS_2 lateral heterostructure with a well-defined heterointerface.

© 2018 WILEY-VCH Verlag GmbH & Co. KGaA, Weinheim

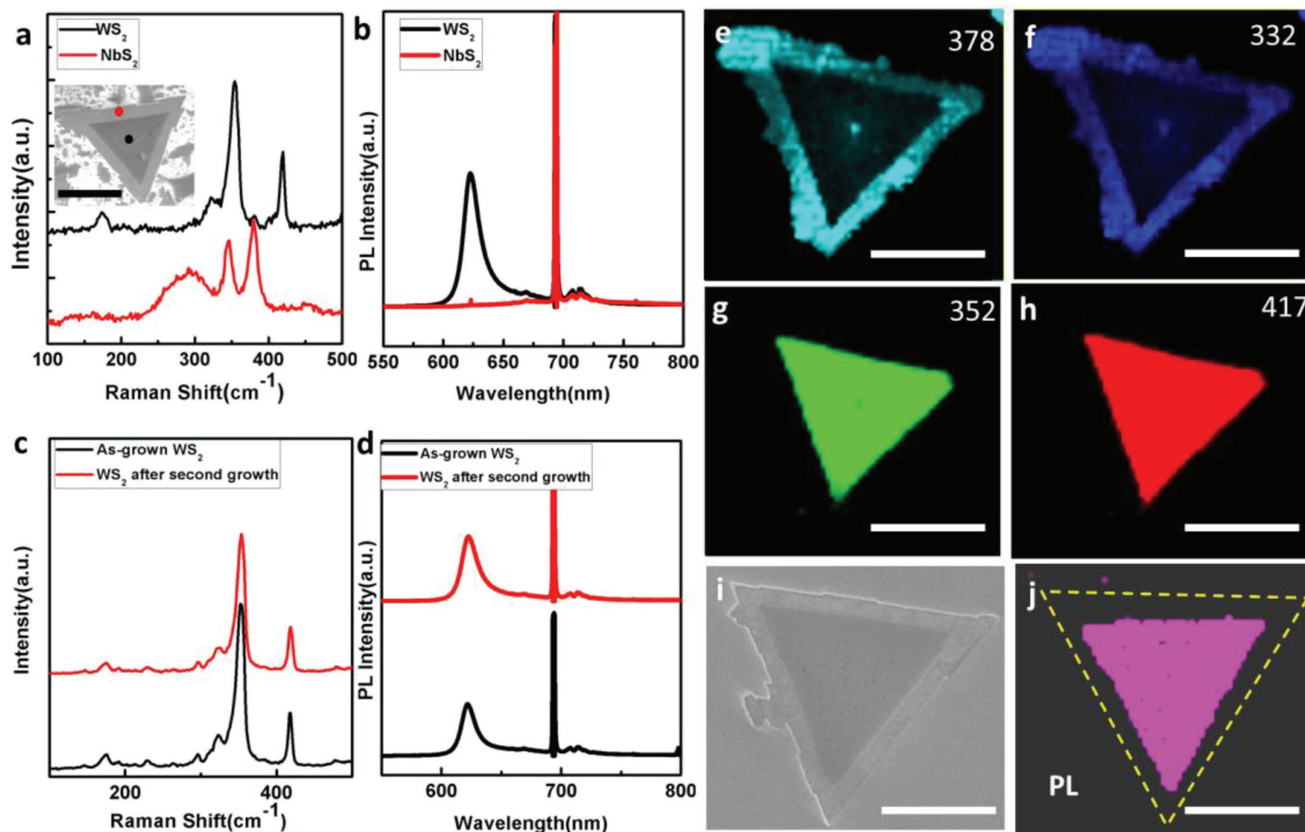

Figure 3. Raman and photoluminescence (PL) characterizations of NbS_2-WS_2 lateral heterostructure. a) Raman spectra (514 nm laser excitation) taken at the different regions of the NbS_2-WS_2 lateral heterostructure, inset: a typical SEM image of NbS_2-WS_2 lateral heterostructure domain. b) PL spectra taken at the different regions indicated in the NbS_2-WS_2 lateral heterostructure. c) Characteristic Raman spectra of as-grown WS_2 monolayer and that after the second growth. d) PL characterizations (514 nm laser excitation) of as-grown WS_2 monolayer and that after the second growth. e,f) 2D Raman mapping images based on the intensity of the A_{1g} and E_{2g} modes of NbS_2 region from the NbS_2-WS_2 lateral heterostructure, respectively. g,h) 2D Raman mapping images based on the intensity of the E_{2g} and A_{1g} modes of WS_2 region from the NbS_2-WS_2 lateral heterostructure, respectively. i) A typical SEM image of the NbS_2-WS_2 lateral heterostructure. j) 2D PL mapping image taken from (i). All the scale bars: 20 µm.

Raman and PL spectra were further conducted to examine the sequential distribution of the chemical composition as well as the local optical properties within the NbS_2-WS_2 lateral heterostructures. **Figure 3**a shows the Raman spectra acquired at different regions within NbS_2-WS_2 heterostructure domain as marked by black and red dots in the SEM image (inset of Figure 3a). The Raman spectrum from the central part presents two characteristic peaks at 352 cm^{-1} (E_{2g}) and 417 cm^{-1} (A_{1g}) (black line in Figure 3a), in agreement with that of monolayer WS_2. Interestingly, the peripheral part (red line in Figure 3a) exhibits quite different features, whose two Raman modes located at 332 cm^{-1} (E_{2g}) and 378 cm^{-1} (A_{1g}) correspond to the typical Raman modes of NbS_2 layers.[31,32] These Raman spectra indicate high quality of the two materials in concentric triangular domain and emphasize the formation of NbS_2-WS_2 lateral heterostructure without compositional alloying. Figure 3b displays the PL spectra collected from WS_2 and NbS_2 regions. The centric WS_2 region exhibits a very strong PL characteristic peak at ≈625 nm, in accordance with an exciton emission of monolayer WS_2 (black line in Figure 3b). However, the peripheral NbS_2 has no PL peak (red line in Figure 3b) due to its metallic nature. Note that the emission around 700 nm originates from the sapphire substrate. Hence, PL spectra also confirm the formation of NbS_2-WS_2 lateral heterostructure. In order to further solidify our observations made above, the Raman and PL spectra of as-grown WS_2 and WS_2 after "step 2" in APCVD was studied for the sake of comparisons (black line and red line in Figure 3c). The peak positions of two prominent peaks for monolayer WS_2 have no deviation. Raman spectra in Figure 3c reveal the same characteristic peaks of WS_2 with no Raman shifts. Similarly, the typical PL peaks for WS_2 at both conditions also possess the same position and intensity as shown in Figure 3d. These results suggest that WS_2 region in the NbS_2-WS_2 lateral heterostructure domain still maintain its intrinsic structure with no doping possibility by other atoms or damage after "step 2" growth. Figure 3e–h exhibits the Raman maps constructed by integrating correlated Raman peak intensities (378 cm^{-1} and 332 cm^{-1} for NbS_2; 351 cm^{-1} and 417 cm^{-1} for WS_2). The clear boundaries demonstrate individual NbS_2 and WS_2 regions, highly verifying the formation of NbS_2-WS_2 lateral heterostructures without any alloy phases in the interface. And uniform signals in the Raman mapping images confirm the high crystalline quality and uniform chemical distribution. The PL mapping image of

© 2018 WILEY-VCH Verlag GmbH & Co. KGaA, Weinheim

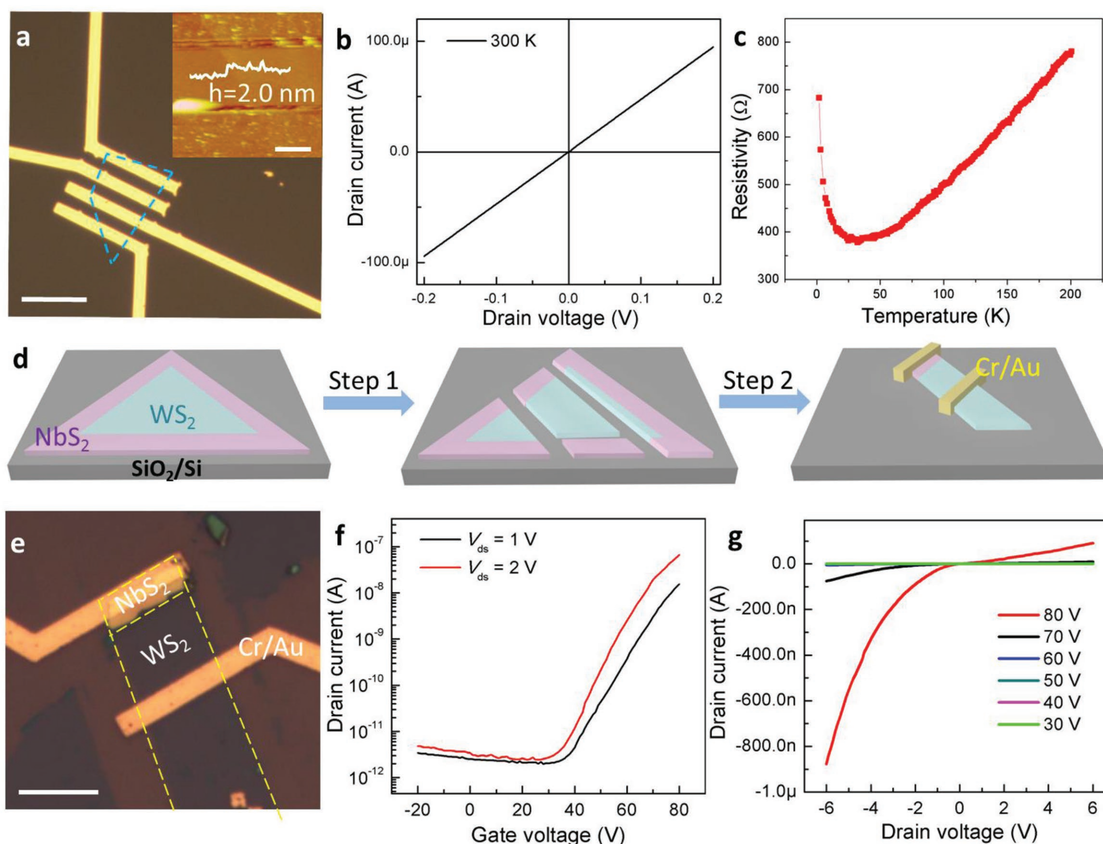

Figure 4. Electrical characterization of NbS_2 flakes and as-grown NbS_2-WS_2 lateral heterostructure. a) The OM image of fabricated device based on as-grown NbS_2 on sapphire. Scale bar, 10 µm. The inset is the AFM image of NbS_2 flake, showing a thickness of ≈2 nm. Scale bar, 10 µm. b) The I_{ds}–V_{ds} curve of the NbS_2 device collected at room temperature. c) Temperature dependence of the resistance for the NbS_2 device. d) Schematic views of the fabrication processes for the FET device based on NbS_2-WS_2 lateral heterostructure domains. e) An optical image of fabricated NbS_2-WS_2 lateral heterostructure device. Scale bar, 10 µm. f) The transfer characteristic curve of this device, demonstrating n-type behavior. g) The corresponding I_{ds}–V_{ds} output characteristics at different backgate voltages.

an NbS_2-WS_2 heterostructure domain in Figure 3i also shows very different PL peaks at 625 nm from the central part while no peak from the out peripheral part, powerfully confirming the sharp interfaces (Figure 3j). In general, the integrated Raman and PL studies of the heterostructures reveal the formation of concentric triangular domains of WS_2 and NbS_2.

To further investigate the transport properties of obtained NbS_2 crystals, electronic devices based on NbS_2 were fabricated on sapphire substrates. **Figure 4**a shows a typical optical image of constructed device of NbS_2 with a thickness of ≈2 nm (shown as inset AFM image). Figure 4b demonstrates a linear I_{ds}–V_{ds} curve collected at room temperature with a resistance of ≈2100 Ω, indicating an Ohmic contact between NbS_2 and electrodes. Figure 4c shows the temperature-dependent resistance of the NbS_2 device, exhibiting a decreasing resistance from 200 to 30 K and then an increasing resistance from 30 to 2 K. The temperature of the minimum resistance (T_m) was observed as ≈30 K and higher than that of bulk NbS_2, which may be due to electron–electron interaction enhanced in low dimensional system.[33] These results confirm the metallic nature of NbS_2 crystals, in a good agreement with DFT calculation.[34] The metallic ground state of NbS_2 crystals is also evidenced by the PL spectra without signal (Figure S3, Supporting Information).

Further, to characterize the electrical transport properties and performance of the obtained NbS_2-WS_2 lateral vdW heterostructures, series of FETs were fabricated on Si substrate with SiO_2 of 300 nm. Figure 4d schematically illustrates the process of device construction. First, the concentric triangular NbS_2-WS_2 lateral heterostructure should be etched by reactive ion etching technique, obtaining an NbS_2-WS_2 lateral heterostructure ribbon. Subsequently, Cr/Au thin films were thermally evaporated as electrodes deposited on NbS_2 region and WS_2 region separately. The detailed fabrication procedure is given in the Experimental Section. Figure 4e shows an optical image of our fabricated FET device based on the NbS_2-WS_2 lateral heterostructure (the thickness of NbS_2 part is shown in Figure S15, Supporting Information). The transfer characteristic curve (I_{ds}–V_{gs}) of this device (Figure 4f) shows a typical n-type behavior with an on–off ratio of 10^5. The field-effect mobility is calculated to be 0.14 $cm^2\ V^{-1}\ s^{-1}$ (L = 9.3 µm, W = 10.9 µm, V_{ds} = 1 V), which is comparable with reported CVD-grown heterostructure result.[38] The corresponding output characteristic (I_{ds}–V_{ds}) in Figure 4g depicts that the I_{ds} decreases with the V_{gs} varying from 80 to 30 V. Most importantly, the gate-tunable output curves demonstrate explicit current rectification behavior, different from that of pure WS_2 (Figure S16, Supporting Information), highly

© 2018 WILEY-VCH Verlag GmbH & Co. KGaA, Weinheim

confirming the formation of Schottky junction across the interface. Even though the complicated device fabrication processes should influence our device properties, our predicted result will be realized after optimizing the technology in our next work. The finding obtained here tangibly corroborates that NbS_2-WS_2 lateral heterostructures broaden the potential application in electronic devices.

In summary, we have demonstrated the controllable CVD-growth of monolayer metallic NbS_2 triangles with their domain sizes reaching up to millimeter scale. More importantly, we realize the epitaxial growth of NbS_2-WS_2 heterostructures in both vertical and lateral ways via a "two-step" CVD method. To our best knowledge, it is a direct synthesis of lateral metal-semiconductor heterostructure reported for the first time. Transmission electron microscope studies have shown the perfect atomic structures and diffraction spots without rotation, highly indicating the clear interface and epitaxial growth behavior of NbS_2-WS_2 lateral heterostructures. Raman and PL studies have further demonstrated the obvious chemical modulation and clear interfaces at the NbS_2-WS_2 lateral heterostructure. Field effect transistors based on the NbS_2-WS_2 lateral heterostructure domains were fabricated. The electronic transport performance has exhibited a well-defined rectification. This work makes a significant step forward, which could expand the range of new heteromaterials and provide more potential applications in electronic devices.

Experimental Section

Synthesis of Monolayer NbS_2 and NbS_2-WS_2 Lateral Heterostructures: An APCVD system was used for the NbS_2 synthesis. A three-zone furnace system was adopted in which Niobium pentoxide (Nb_2O_5) powder (Alfa Aesar, purity 99%) and sulfur (S) powder (Alfa Aesar, purity 99.5%) were used as precursors. Two quartz boats containing S, Nb_2O_5, and substrates were loaded into the tube from upstream to downstream with the temperature of 190 and 790 °C, respectively. The substrates were faced downward on the Nb_2O_5 powder (0.5 g) mixed with a little amount of sodium chloride (NaCl (0.05 g)). Prior to heating, the furnace tube was purged with 400 sccm Ar for 30 min and then with 100 sccm Ar and 1–10 sccm H_2 to create a preferable growth atmosphere for the growth. The NbS_2 growth lasted for 15 min and finally NbS_2 monolayer was obtained on sapphire substrates.

For the synthesis of NbS_2-WS_2 lateral heterostructure, monolayer WS_2 flakes were first synthesized via APCVD method. S powder was placed at the upstream of furnace, tungsten trioxide (WO_3) powder (Alfa Aesar, purity 99.9%) and sapphire (Al_2O_3(0001)) substrates were successively placed at the center of furnace. The evaporating temperature of S and WO_3 were 150 and 730 °C, respectively. Prior to heating, the furnace tube was purged with 400 sccm Ar for 30 min and the reaction time was about 10 min. Finally, WS_2 monolayer was obtained on sapphire substrates. The sapphire substrate, onto which the WS_2 monolayers were grown, was used as substrate for the second step growth of metallic NbS_2. Eventually, epitaxially grown lateral NbS_2-WS_2 heterostructure was obtained.

Transfer of As-Grown NbS_2 and NbS_2-WS_2 Lateral Heterostructures: The as-grown samples were spin-coated with poly(methyl methacrylate) (PMMA; 495 K, A4, Microchem Company) at a speed of 1500 rpm for 45 s followed by drying at 180 °C for 10 min. Then the samples supported by PMMA film were lifted up by tweezers under the water and it was then collected by a target substrate. Finally, the PMMA film was removed via dissolution with acetone for about 30 min and dried by the flowing N_2 gas.

Characterizations of As-Grown NbS_2 and NbS_2-WS_2 Lateral Heterostructures: The morphologies of NbS_2 and NbS_2-WS_2 lateral heterostructures were characterized by optical microscope (OM, Olympus BX51M), Hitach S-4800 scanning electron microscope, Tecnai F20 transmission electron microscope, and Titan G2 60–300 Probe Cs Corrector HRSTEM. STEM-EDX elemental mapping was characterized by Tecnai F20. The thickness of obtained samples was characterized by atomic force microscope (Bruker Icon). The temperature-dependent Raman and PL spectra were obtained from confocal microscope-based Raman spectrometer (Renishaw InVia, 514 nm excitation laser). X-ray photoelectron spectroscopy was tested on ESCALAB 250 Xi.

Fabrications and Measurement of the As-Grown NbS_2 and NbS_2-WS_2 Devices: The as-grown NbS_2 flakes on sapphire were fabricated into devices without transfer. The standard electron-beam lithography (EBL) processing was used to define the source/drain electrodes. To avoid charge accumulation on the insulating sapphire substrate during EBL, a layer of conductive coating (AR-PC, 5090.02) was spin-coated on the sapphire substrate with NbS_2 flakes before spin-coating PMMA (495 K). Subsequently, Cr/Au metal layer (Cr: 8 nm, Au: 50 nm) was deposited to form electrodes by thermal evaporation. Room-temperature measurements were performed with a semiconductor parameter analyzer (Keithley Model 4200-SCS). Temperature dependence of resistivity was performed using the Physical Properties Measurement Systems (Quantum Design) with temperature ranging from 200 to 2 K.

The as-grown NbS_2-WS_2 lateral heterostructures were transferred from sapphire substrate to SiO_2/Si for the fabrication of FET devices. After this, a layer of PMMA was spin-coated on the substrate followed by a 3 min bake at 120 °C. Standard EBL technique was employed to prepare the source/drain electrodes. Then 8 nm Cr and 50 nm Au were thermally evaporated as electrodes and followed by lift-off process with acetone. All of the measurements were performed on a probe station (Lakeshore, TTP4) with vacuum of 10^{-6} torr. The data were collected by Keithley 4200 semiconductor parameter analyzer.

Supporting Information

Supporting Information is available from the Wiley Online Library or from the author.

Acknowledgements

This work was supported by Ministry of Science and Technology of China (Grant No. 2016YFA0200700), National Natural Science Foundation of China (Grant Nos.61625401, 21703047, 61474033, 61574050, 11674072, and 11704389), Strategic Priority Research Program of the Chinese Academy of Sciences (Grant No. XDA09040201), and CAS Key Laboratory of Nanosystem and Hierarchical Fabrication. The authors also gratefully acknowledge the support of Youth Innovation Promotion Association CAS.

Conflict of Interest

The authors declare no conflict of interest.

Keywords

controllable growth, metallic transition metal dichalcogenides (TMDs), metal-semiconductor heterostructures, NbS_2-WS_2 heterostructures

Received: June 9, 2018
Revised: July 16, 2018
Published online:

© 2018 WILEY-VCH Verlag GmbH & Co. KGaA, Weinheim

[1] T. Yokoya, T. Kiss, A. Chainani, S. Shin, M. Nohara, H. Takagi, *Science* **2001**, *294*, 2518.
[2] B. Sipos, A. F. Kusmartseva, A. Akrap, H. Berger, L. Forro, E. Tutis, *Nat. Mater.* **2008**, *7*, 960.
[3] R. Ang, Y. Tanaka, E. Ieki, K. Nakayama, T. Sato, L. J. Li, W. J. Lu, Y. P. Sun, T. Takahashi, *Phys. Rev. Lett.* **2012**, *109*, 176403.
[4] K. Xu, P. Z. Chen, X. L. Li, C. Z. Wu, Y. Q. Guo, J. Y. Zhao, X. J. Wu, Y. Xie, *Angew. Chem., Int. Ed.* **2013**, *52*, 10477.
[5] X. Zhu, Y. Guo, H. Cheng, J. Dai, X. An, J. Zhao, K. Tian, S. Wei, X. C. Zeng, C. Wu, *Nat. Commun.* **2016**, *7*, 11210.
[6] M. Eichberger, H. Schafer, M. Krumova, M. Beyer, J. Demsar, H. Berger, G. Moriena, G. Sciaini, R. J. D. Miller, *Nature* **2010**, *468*, 799.
[7] J. A. Wilson, F. J. Di Salvo, S. Mahajan, *Adv. Phys.* **2001**, *50*, 1171.
[8] U. Chatterjee, J. Zhao, M. Iavarone, R. D. Capua, J. P. Castellan, G. Karapetrov, C. D. Malliakas, M. G. Kanatzidis, H. Claus, J. P. C. Ruff, *Nat. Commun.* **2015**, *6*, 6313.
[9] B. Radisavljevic, A. Radenovic, J. Brivio, V. Giacometti, A. Kis, *Nat. Nanotechnol.* **2011**, *6*, 147.
[10] M. Chhowalla, H. S. Shin, G. Eda, L. J. Li, K. P. Loh, H. Zhang, *Nat. Chem.* **2013**, *5*, 263.
[11] A. M. van der Zande, P. Y. Huang, D. A. Chenet, T. C. Berkelbach, Y. M. You, G. H. Lee, T. F. Heinz, D. R. Reichman, D. A. Muller, J. C. Hone, *Nat. Mater.* **2013**, *12*, 554.
[12] J. Chen, X. Zhao, S. J. R. Tan, H. Xu, B. Wu, B. Liu, D. Fu, W. Fu, D. Geng, Y. Liu, W. Liu, W. Tang, L. Li, W. Zhou, T. C. Sum, K. P. Loh, *J. Am. Chem. Soc.* **2017**, *139*, 1073.
[13] T. Zhang, B. Jiang, Z. Xu, R. G. Mendes, Y. Xiao, L. F. Chen, L. W. Fang, T. Gemming, S. L. Chen, M. H. Rummeli, L. Fu, *Nat. Commun.* **2016**, *7*, 13911.
[14] L. Zhou, K. Xu, A. Zubair, A. D. Liao, W. J. Fang, F. P. Ouyang, Y. H. Lee, K. Ueno, R. Saito, T. Palacios, J. Kong, M. S. Dresselhaus, *J. Am. Chem. Soc.* **2015**, *137*, 11892.
[15] M. M. Ugeda, A. J. Bradley, Y. Zhang, S. Onishi, Y. Chen, W. Ruan, C. Ojedaaristizabal, H. Ryu, M. T. Edmonds, H. Tsai, *Nat. Phys.* **2015**, *12*, 92.
[16] Y. J. Yu, F. Y. Yang, X. F. Lu, Y. J. Yan, Y. H. Cho, L. G. Ma, X. H. Niu, S. Kim, Y. W. Son, D. L. Feng, S. Y. Li, S. W. Cheong, X. H. Chen, Y. B. Zhang, *Nat. Nanotechnol.* **2015**, *10*, 270.
[17] J. P. Shi, X. N. Wang, S. Zhang, L. F. Xiao, Y. H. Huan, Y. Gong, Z. P. Zhang, Y. C. Li, X. B. Zhou, M. Hong, Q. Y. Fang, Q. Zhang, X. F. Liu, L. Gu, Z. F. Liu, Y. F. Zhang, *Nat. Commun.* **2017**, *8*, 958.
[18] Q. Q. Ji, C. Li, J. L. Wang, J. J. Niu, Y. Gong, Z. P. Zhang, Q. Y. Fang, Y. Zhang, J. P. Shi, L. Liao, X. S. Wu, L. Gu, Z. F. Liu, Y. F. Zhang, *Nano Lett.* **2017**, *17*, 4908.
[19] X. X. Xi, L. Zhao, Z. F. Wang, H. Berger, L. Forro, J. Shan, K. F. Mak, *Nat. Nanotechnol.* **2015**, *10*, 765.
[20] H. Wang, X. W. Huang, J. H. Lin, J. Cui, Y. Chen, C. Zhu, F. C. Liu, Q. S. Zeng, J. D. Zhou, P. Yu, X. W. Wang, H. Y. He, S. H. Tsang, W. B. Gao, K. Suenaga, F. C. Ma, C. L. Yang, L. Lu, T. Yu, E. H. T. Teo, G. T. Liu, Z. Liu, *Nat. Commun.* **2017**, *8*, 394.
[21] R. Zhao, Y. Wang, D. Deng, X. Luo, W. J. Lu, Y. P. Sun, Z. K. Liu, L. C. Chen, J. Robinson, *Nano Lett.* **2017**, *17*, 3471.
[22] S. Bae, H. Kim, Y. Lee, X. F. Xu, J. S. Park, Y. Zheng, J. Balakrishnan, T. Lei, H. R. Kim, Y. I. Song, Y. J. Kim, K. S. Kim, B. Ozyilmaz, J. H. Ahn, B. H. Hong, S. Iijima, *Nat. Nanotechnol.* **2010**, *5*, 574.
[23] H. G. Shin, H. S. Yoon, J. S. Kim, M. Kim, J. Y. Lim, S. Yu, J. H. Park, Y. Yi, T. Kim, S. C. Jun, *Nano Lett.* **2018**, *18*, 1937.
[24] H. J. Chuang, B. P. Chamlagain, M. Koehler, M. M. Perera, J. Yan, D. Mandrus, D. Tomanek, Z. Zhou, *Nano Lett.* **2016**, *16*, 1896.
[25] A. R. Kim, Y. Kim, J. Nam, H. S. Chung, D. J. Kim, J. D. Kwon, S. W. Park, J. Park, S. Y. Choi, B. H. Lee, *Nano Lett.* **2016**, *16*, 1890.
[26] A. Allain, J. Kang, K. Banerjee, A. Kis, *Nat. Mater.* **2015**, *14*, 1195.
[27] J. Yuan, J. Wu, W. J. Hardy, P. Loya, M. Lou, Y. Yang, S. Najmaei, M. Jiang, F. Qin, K. Keyshar, *Adv. Mater.* **2015**, *27*, 5605.
[28] C. Liu, R. F. Frindt, *Phys. Rev. B* **1985**, *31*, 4086.
[29] Y. G. Zhou, Z. G. Wang, P. Yang, X. T. Zu, L. Yang, X. Sun, F. Gao, *ACS Nano* **2012**, *6*, 9727.
[30] J. A. Wilson, A. D. Yoffe, *Adv. Phys.* **1969**, *18*, 193.
[31] X. Wang, J. Lin, Y. Zhu, C. Luo, K. Suenaga, C. Cai, L. Xie, *Nanoscale* **2017**, *9*, 16607.
[32] W. Ge, K. Kawahara, M. Tsuji, H. Ago, *Nanoscale* **2013**, *5*, 5773.
[33] S. H. Zhao, T. Hotta, T. Koretsune, K. Watanabe, T. Taniguchi, K. Sugawara, T. Takahashi, H. Shinohara, R. Kitaura, *2D Mater.* **2016**, *3*, 025027.
[34] A. Kuc, N. Zibouche, T. Heine, *Phys. Rev. B* **2011**, *83*, 2237.
[35] Y. Liu, P. Stradins, S. H. Wei, *Sci. Adv.* **2016**, *2*, e1600069.
[36] H. Katsuta, R. B. Mclellan, K. Suzuki, *J. Phys. Chem. Solids* **1979**, *40*, 1089.
[37] Y. Zhao, J. Qiao, P. Yu, Z. Hu, Z. Lin, S. P. Lau, Z. Liu, W. Ji, Y. Chai, *Adv. Mater.* **2016**, *28*, 2399.
[38] Y. Zhao, J. Qiao, Z. Yu, P. Yu, K. Xu, S. P. Lau, W. Zhou, Z. Liu, X. Wang, W. Ji, *Adv. Mater.* **2017**, *29*, 1604230.
[39] Z. Zhang, J. Niu, P. Yang, G. Yue, Q. Ji, J. Shi, Q. Fang, S. Jiang, L. He, X. Zhou, *Adv. Mater.* **2017**, *29*, 1702359.
[40] T. Yang, B. Zheng, Z. Wang, T. Xu, C. Pan, J. Zou, X. Zhang, Z. Qi, H. Liu, Y. Feng, *Nat. Commun.* **2017**, *8*, 1906.
[41] Y. Zhang, Y. Zhang, Q. Ji, J. Ju, H. Yuan, J. Shi, T. Gao, D. Ma, M. Liu, Y. Chen, *ACS Nano* **2013**, *7*, 8963.
[42] Y. Gong, J. Lin, X. Wang, G. Shi, S. Lei, Z. Lin, X. Zou, G. Ye, R. Vajtai, B. I. Yakobson, *Nat. Mater.* **2014**, *13*, 1135.
[43] K. K. Liu, W. Zhang, Y. H. Lee, Y. C. Lin, M. T. Chang, C. Y. Su, C. S. Chang, H. Li, Y. Shi, H. Zhang, *Nano Lett.* **2012**, *12*, 1538.
[44] M. Y. Li, Y. M. Shi, C. C. Cheng, L. S. Lu, Y. C. Lin, H. L. Tang, M. L. Tsai, C. W. Chu, K. H. Wei, J. H. He, W. H. Chang, K. Suenaga, L. J. Li, *Science* **2015**, *349*, 524.
[45] P. K. Sahoo, S. Memaran, X. Yan, L. Balicas, H. R. Gutiérrez, *Nature* **2018**, *553*, 63.
[46] Y. J. Gong, J. H. Lin, X. L. Wang, G. Shi, S. D. Lei, Z. Lin, X. L. Zou, G. L. Ye, R. Vajtai, B. I. Yakobson, H. Terrones, M. Terrones, B. K. Tay, J. Lou, S. T. Pantelides, Z. Liu, W. Zhou, P. M. Ajayan, *Nat. Mater.* **2014**, *13*, 1135.
[47] J. Zhou, J. Lin, X. Huang, Y. Zhou, Y. Chen, J. Xia, H. Wang, Y. Xie, H. Yu, J. Lei, *Nature* **2018**, *556*, 355.
[48] J. H. Sung, H. Heo, S. Si, Y. H. Kim, H. R. Noh, K. Song, J. Kim, C. S. Lee, S. Y. Seo, D. H. Kim, *Nat. Nanotechnol.* **2017**, *12*, 1064.
[49] Q. Fu, X. Wang, J. Zhou, J. Xia, Q. Zeng, D. Lv, C. Zhu, X. Wang, Y. Shen, X. Li, Y. Hua, F. Liu, Z. Shen, C. Jin, Z. Liu, *Chem. Mater.* **2018**, *30*, 4001.
[50] V. D. Z. Am, P. Y. Huang, D. A. Chenet, T. C. Berkelbach, Y. You, G. H. Lee, T. F. Heinz, D. R. Reichman, D. A. Muller, J. C. Hone, *Nat. Mater.* **2013**, *12*, 554.
[51] X. Ling, Y. H. Lee, Y. Lin, W. Fang, L. Yu, M. S. Dresselhaus, J. Kong, *Nano Lett.* **2014**, *14*, 464.
[52] X. Duan, C. Wang, J. C. Shaw, R. Cheng, Y. Chen, H. Li, X. Wu, Y. Tang, Q. Zhang, A. Pan, *Nat. Nanotechnol.* **2014**, *9*, 1024.

© 2018 WILEY-VCH Verlag GmbH & Co. KGaA, Weinheim